Ventilation of the Equatorial Atlantic by the Equatorial Deep Jets

Peter Brandt[1], Richard J. Greatbatch[1], Sven-Helge Didwischus[1], Martin Claus[1], Verena Hormann[2], Andreas Funk[1,3], Johannes Hahn[1], Gerd Krahmann[1], Jürgen Fischer[1], Arne Körtzinger[1]

[1]GEOMAR Helmholtz-Zentrum für Ozeanforschung Kiel, Düsternbrooker Weg 20, 24105 Kiel, Germany

[2]Cooperative Institute for Marine and Atmospheric Studies, University of Miami, and National Oceanic and Atmospheric Administration/Atlantic Oceanographic and Meteorological Laboratory, Miami, FL 33149, USA

[3]now at WTD 71, Forschungsbereich für Wasserschall und Geophysik FWG, 24148 Kiel, Germany

Abstract

Equatorial deep jets (EDJs) are a prominent flow feature of the equatorial Atlantic below the Equatorial Undercurrent down to about 3000 m. Here we analyze long-term moored velocity and oxygen observations, as well as shipboard hydrographic and current sections acquired along 23°W and covering the depth range of the oxygen minimum zones of the eastern tropical North and South Atlantic. The moored zonal velocity data show high-baroclinic mode EDJ oscillations at a period of about 4.5 years. Equatorial oxygen observations which do not resolve or cover a full 4.5-yr EDJ cycle nevertheless reveal large variability, with oxygen concentrations locally spanning a range of more than 60 μmol kg^{-1}. We study the effect of EDJs on the equatorial oxygen concentration by forcing an advection-diffusion model with the velocity field of the gravest equatorial basin mode corresponding to the observed EDJ cycle. The advection-diffusion model includes an oxygen source at the western boundary and oxygen consumption elsewhere. The model produces a 4.5-yr cycle of the oxygen concentration and a temporal phase difference between oxygen concentration and eastward velocity that is less than quadrature, implying a net eastward oxygen flux. The comparison of available observations and basin-mode simulations indicates that a substantial part of the observed oxygen variability at the equator can be explained by EDJ oscillations. The respective role of mean advection, EDJs, and other possible processes in shaping the mean oxygen distribution of the equatorial Atlantic at intermediate depth is discussed.

1. Introduction

Vertically alternating deep zonal jets of short vertical wavelength were discovered in the equatorial oceans more than 30 years ago [*Luyten and Swallow*, 1976]. Observations show them to be coherent across entire equatorial basins [*Ponte and Luyten*, 1990; *Johnson et al.*, 2002; *Johnson and Zhang*, 2003]. These jets, which are also referred to as equatorial deep jets (EDJs), are characterized by vertically alternating eastward and westward currents lying within 1° of the equator, amplitudes of 0.1-0.2 ms^{-1}, and vertical wavelengths between 300 and 700 m. Analysis of different datasets acquired in the equatorial Atlantic including historical hydrographic data covering the period 1972-1998 [*Johnson and Zhang*, 2003], data from single point current meters at moorings deployed during 2000-2006 [*Bunge et al.*, 2008], as well as vertically continuous velocity profiles taken from acoustic Doppler current profilers (ADCPs) and moored profilers deployed during 2004-2009 [*Brandt et al.*, 2011], show consistent interannual oscillations of EDJs with a period of about 4.5 years. These oscillations can be understood in terms of equatorial Kelvin and Rossby wave propagation that form an equatorial basin mode under resonant conditions [*Cane and Moore*, 1981]. General agreement between the space-time structure of EDJs at a given depth and an equatorial basin mode for a high-order baroclinic mode has been found by *Greatbatch et al.* [2012] when including a lateral eddy viscosity of between 200 and 300 $m^2\ s^{-1}$. The oscillatory behavior of EDJs is also found in three-dimensional process studies in which an idealized forcing by intraseasonal waves provides the energy for EDJ generation [*d´Orgeville et al.*, 2007].

The vertical oxygen distribution in the tropical ocean is characterized by an oxygen minimum at intermediate depth separating the well-ventilated near-surface layer from the oxygen-rich deeper

layers. At intermediate depths within the low-oxygen region, the climatological, time-averaged meridional oxygen distribution exhibits a broad maximum in the equatorial band separating the oxygen minimum zones of both hemispheres [*Karstensen et al.*, 2008] (Figure 1), which is generally not captured by state-of-the-art coarse-resolution simulations [*Meissner et al.*, 2005; *Keeling et al.*, 2010; *Duteil and Oschlies*, 2011]. This maximum, however, is well known from observational data and was first discovered during the German Atlantic Meteor expedition 1925-27 [*Wattenberg*, 1939]. The main reason for the failure of coarse resolution models in simulating the equatorial oxygen distribution seems to be the absense of the mean and variable equatorial intermediate current system [*Ascani et al.*, 2010;.*Duteil and Oschlies*, 2011]. At intermediate depths (300-700 m), the mean flow is composed of narrow zonal currents (Figures 1 and 2a) including the westward flowing Equatorial Intermediate Current (EIC) centered on the equator between the eastward Southern and Northern Intermediate Countercurrents (SICC, NICC) located at about 2°S and 2°N, respectively [e.g., *Brandt et al.*, 2006]. The mean eastward flow of the NICC and SICC has been recognized to ventilate the eastern tropical Atlantic by transporting oxygen-rich waters from the well-ventilated western boundary toward the east [*Tsuchiya et al.*, 1992; *Schott et al.*, 1998; *Stramma et al.*, 2005]. At the equator, the superposition of the mean westward flow which carries low-oxygen water westward [*Schott et al.*, 1998] and the EDJs can result in intermittent flow reversals on interannual time scales. *Brandt et al.* [2008] observed an oxygen tongue at the equator in the depth interval of the EIC extending from 35°W to 10°W that has been explained by the presence of an eastward jet during the preceding year. Moreover, they found that the eastward reduction in oxygen within the eastward progressing tongue was mainly due to meridional diffusion; vertical diffusion and oxygen consumption were found to play a

minor role. These observations suggest an eastward and poleward oxygen flux by the combination of oscillating EDJs and horizontal diffusion. Other processes that might play a role for the ventilation of the equatorial Atlantic are vertical mixing and wave-induced stirring. The latter mechanism was suggested by *Li et al.* [1996] and results from tracer advection by the flow field caused by the superposition of at least two different equatorial waves, in their case the combination of annual Rossby waves and intraseasonal mixed Rossby-gravity waves. It is also possible that the Stokes drift associated with velocity fluctuations in the equatorial region might play a role, modifying the oxygen advection that is implied by the Eulerian mean flow (see, for example, *Moore* [1970] and *Ascani et al.* [2010]).

The description of long-term (i.e., decadal to multi-decadal) variability of oxygen concentrations in the open ocean typically relies on shipboard measurements [*Garcia et al.*, 2005; *Johnson and Gruber*, 2007; *Stramma et al.*, 2008]. However, the analysis of shorter period fluctuations is in general limited by the amount of available shipboard data which are typically not able to resolve oxygen fluctuations on intraseasonal to interannual time scales. A rare example of continuous oxygen observations in the open ocean is the oxygen time series obtained at Ocean Station Papa (50°N, 145°W) from weather ships and research vessels since 1956. This time series revealed declining overall oxygen concentrations and fluctuations on time scales of a few years to bi-decadal [*Whitney et al.*, 2007].

The mean oxygen and velocity distributions and their interannual variability are analyzed in sections 2 and 3 using long-term velocity measurements from equatorial Atlantic moorings, with oxygen measurements taken during a single 1.5-yr mooring period, as well as velocity and water mass observations from cross-equatorial shipboard sections along ~23°W taken during 2006-

2011. To corroborate the hypothesis that the observed interannual oxygen variability in the equatorial Atlantic is due to EDJ oscillations an advection-diffusion model forced by the velocity field of the gravest equatorial basin mode [*Greatbatch et al.*, 2012] is used (section 4); it includes restoring to high oxygen concentrations in the western boundary region and oxygen consumption elsewhere. Finally, the results of this study regarding the role of EDJ oscillations for the oxygen distribution and variability in the equatorial Atlantic are summarized and discussed (section 5).

2. Observed Mean Oxygen and Velocity along 23°W

The mean oxygen concentration and zonal velocity along 23°W as obtained from recent ship sections (Figure 2) were discussed in detail in *Brandt et al.* [2010]; further information on the datasets used in the present study are given in Appendix A. Here, we focus on the relation of the mean oxygen distribution and zonal currents in the equatorial band. Considering the general zonal gradient in the mean oxygen distribution (Figure 1), one would expect eastward and westward flow to be associated with high and low oxygen concentrations, respectively. This is approximately the case for the flow in the upper 250 m below the well-ventilated near-surface layer. The eastward flowing Equatorial Undercurrent (EUC), the South Equatorial Undercurrent (SEUC) at 4.5°S, and the weaker North Equatorial Undercurrent (NEUC) at 5°N are all characterized by oxygen maxima, with oxygen minima in between (Figures 2 and 3a). Despite the pronounced zonal flow pattern below 250 m a similar behavior of the oxygen distribution cannot be observed. Analysis of the meridional structures of oxygen and zonal velocity at 300 m (Figure 3b) and 500 m (Figure 3c) shows at 300 m 1) a strong equatorial asymmetry with eastward velocities of the SEUC and NICC and westward velocities in between, mainly south of

the equator between 1°S and 3.5°S; 2) an oxygen maximum associated with the SEUC and an oxygen maximum that should be associated with the NICC but is shifted toward the equator by about 1° latitude. At 500 m the data show 1) a symmetric velocity field with respect to the equator, and 2) a broad oxygen maximum between the cores of the NICC and SICC at about 2°N and 2°S, respectively. In both cases, the increase of the mean oxygen concentration toward the equator is not consistent with oxygen advection by the mean zonal current bands and other processes must come into play. Such processes may include mean ventilation by EDJs, which is a focus of this study, vertical mixing, wave-induced stirring, or a Stokes drift opposing the Eulerian mean flow.

The vertical profile of the mean zonal velocity as obtained from more than seven years of mooring data indicates a two-core structure of the westward flowing EIC (Figure 4). A similar structure was already found by *Brandt et al.* [2006] using only the first 16 months of the present time series. We have here not taken into account a possible bias of the mean due to the presence of EDJs (an issue discussed further in the next section). The upper core of westward flow is located at about 245 m, while the lower core is observed at 435 m depth. At about 300 m, there is a weak mean eastward flow. The minimum oxygen concentration at the equator is found at about 280 m (Figure 4), much shallower than the core of the oxygen minimum zones of both hemispheres [*Karstensen et al.*, 2008; *Brandt et al.*, 2010].

3. Interannual Variability

a) Time series

The zonal velocity as obtained from moored observations at the equator, 23°W from February

2004 to June 2011 is shown in Figure 5. This dataset represents an update of data published by *Brandt et al.* [2011]. The primary signal in the near-surface layer is the eastward flowing EUC with its pronounced seasonal cycle. Below the EUC, seasonal and interannual variations dominate the zonal velocity field. By fitting a 1670-d harmonic cycle to the zonal velocity data below the EUC and displaying the 0° and 180° phase lines as done by *Brandt et al.* [2011], the downward phase propagation of high-baroclinic mode EDJs becomes evident (Figure 5); similar downward phase propagation was found in other observations by *Johnson and Zhang* [2003] and *Bunge et al.* [2008]. The zonal velocities at 300 and 500 m depth have amplitudes for the 1670-d harmonic cycle of about 9.3±3.0 cm s^{-1} and 10.7±3.5 cm s^{-1}, respectively (Figure 6). As the length of the moored time series is not an integer multiple of the EDJ period, the EDJ cycle might bias the means presented in Figure 4. When subtracting the 1670-d harmonic cycle calculated at each depth from the moored zonal velocity time series, a mean zonal velocity of the residual can be derived that is −1.4±2.9 cm s^{-1} at 300 m and −4.7±2.8 cm s^{-1} at 500 m, which differs from values of +1.1±4.3 cm s^{-1} and −6.4±5.0 cm s^{-1} derived without subtracting the EDJ cycle. The local eastward velocity maximum at about 300 m as observed in Figure 4 is reduced when accounting for the bias due to the EDJ cycle. Nevertheless, the mean zonal velocity appears to be more strongly westward at 500 m than at 300 m which is consistent with the mean zonal velocity from the longer though more scattered time series of shipboard data (Figure 2a).

Although the moored oxygen data do not cover a full EDJ cycle, these data show that the oxygen variability at 300 m depth is dominated by the EDJ cycle (Figure 6a). There is an almost steady increase in the oxygen concentration at 300 m depth from November 2009 to November 2010 during a phase of strong eastward flow associated with the EDJ cycle. After the zonal velocity

turns to westward flow in November 2010, the increase in oxygen concentration stops and it decreases rapidly in February 2011. During almost the whole mooring period from November 2009 to May 2011, the oxygen concentration was well above the mean oxygen concentration of 103±5 μmol kg^{-1} estimated from the ship sections. Taking into account the short oxygen time series from February 2008 which was acquired shortly after maximum westward velocity of the EDJ cycle, the total range of oxygen variability at 300 m depth is more than 60 μmol kg^{-1} - well above the measurement error of about 3 μmol kg^{-1} (Appendix A). This represents a large interannual variability in the central equatorial Atlantic Ocean at intermediate depth which can be ascribed to the presence of EDJs.

The variability of the oxygen concentration at 500 m depth (Figure 6b) appears to be substantially different from the one found at 300 m depth. The oxygen concentration varies only slightly around the mean value of 129±3 μmol kg^{-1} estimated from the ship sections. The total range of oxygen variability from the mooring data is less than 20 μmol kg^{-1} and varies here mainly on shorter periods. Why is the behavior of the oxygen concentration so different at 300 and 500 m depth? The velocity amplitude of the EDJ cycle is similar at both depths - even slightly larger at 500 m depth. A factor that could affect the oxygen variability is the zonal oxygen gradient along the equator. The climatological difference between the oxygen concentrations at the western and eastern boundaries (as a proxy of the zonal oxygen gradient along the equator) is reduced by about one third at 500 m (about 60 μmol kg^{-1}) compared to 300 m depth (about 90 μmol kg^{-1}). This reduction of the zonal oxygen gradient with depth in the equatorial region might be understood as a consequence of a steady-state balance between oxygen consumption declining exponentially with depth [*Karstensen et al.*, 2008] and dominance

of zonal ventilation from the western boundary. The reduced zonal oxygen gradient found at 500 m might thus help to explain the reduced amplitude of oxygen oscillations within the EDJ cycle at that depth compared to the situation at 300 m depth.

b) Cross-equatorial sections

Our moored observations at the equator have suggested that a substantial part of the observed large oxygen variability at 300 m depth is related to the EDJ cycle, while the oxygen variability at 500 m is relatively small. We next analyze the meridional oxygen distribution of hydrographic sections obtained during different research cruises (Figure 7). Here, we use four hydrographic sections that were acquired during mooring deployment and recovery cruises - about 1.5 years apart. Similar to previous studies, these sections indicate large oxygen variability at intermediate depths. The strong equatorial oxygen maximum found in June 2006 at about 330 m depth could be tracked from the western equatorial Atlantic at 35°W to the eastern basin at 10°W during that particular research cruise [*Brandt et al.*, 2008]. The latitudinal and vertical scales of the oxygen tongue correspond approximately to the scales of observed EDJs in the equatorial Atlantic [*Gouriou et al.*, 2001; *Bourlès et al.*, 2003]. Here, we analyze the meridional structure of the oxygen anomaly averaged between 280 and 380 m depth for the four different cruises (Figure 8a). Largest variability is found at the equator, with maximum oxygen concentration during June 2006 and minimum oxygen concentration during February/March 2008, which is in agreement with our expectation from the analysis of the moored velocity time series. The total range of oxygen variability in this depth interval at the equator is in general agreement with the range obtained from moored observations at 300 m depth (cf. Figures 6a and 8a); off-equatorial oxygen anomalies are slightly smaller in amplitude and more irregular.

The second depth interval we analyze here ranges from 450 m to 550 m (Figure 8b). This deeper depth interval is, in comparison with the shallower interval, characterized by a similar amplitude of zonal velocity oscillations, a reduced zonal oxygen gradient along the equator, and a stronger westward mean flow. Consistent with the analysis of the moored observations, the oxygen variability at the equator is reduced in the deeper depth interval as compared to the shallower one (cf. Figures 6b and 8b). However, the off-equatorial oxygen variability at 2-3°S and N is similar or even larger which might be explained by lateral movement of the strong meridional oxygen gradients associated with the NICC and SICC at about 2°N and 2°S, respectively (Figures 2 and 3c).

4. Advection-Diffusion Model

a) Model setup

Greatbatch et al. [2012] have described the space-time structure of EDJs at a given depth using a reduced-gravity model simulating an equatorial basin mode for a high-order baroclinic mode. The simulations were performed for a rectangular basin of width 55° longitude (45°W-10°E) and extending from 10°S to 10°N mimicking the equatorial Atlantic Ocean. The gravity wave speed (0.17 ms^{-1}) was chosen so that the period of observed EDJ oscillations, that is 1670 days, is the same as the period associated with the gravest equatorial basin mode in the model. In *Greatbatch et al.* [2012], the width of the EDJs was found to depend on the lateral eddy viscosity and simulated EDJ widths were consistent with observations when using values of between 200 and 300 $m^2\ s^{-1}$. We use here the steady, oscillating velocity field of the basin-mode simulation for a lateral eddy viscosity of 200 $m^2\ s^{-1}$ to force the following advection-diffusion model:

$$\frac{\partial C}{\partial t} = -JC - \mathbf{u} \cdot \nabla C + k_h \Delta C - R\left(C - C_0\right), \qquad (1)$$

where C is the oxygen concentration, J = 0.041 yr^{-1} is the constant oxygen consumption coefficient as used in previous studies [*van Geen et al.*, 2006; *Brandt et al.*, 2010], $\mathbf{u}$ is the horizontal velocity vector, k_h = 200 m^2 s^{-1} is the coefficient of the horizontal eddy diffusivity, and R^{-1} is the time scale for the oxygen concentration to be restored to the prescribed value C_0 (note that since the model solves for the normalized concentration C/C_0, the value of C_0 in the model is 1). The restoring term is used to introduce a source of oxygen at the western boundary (in reality associated with the oxygen-rich western boundary current, that is the North Brazil Current (NBC) [*Schott et al.*, 2005]). The restoring coefficient, R, is independent of latitude and is given by $R = \gamma/2\left(1 - \tanh\left(\left(x - x_0\right)/L\right)\right)$, where x is longitude with an inflection point, x_0, at 35°W, a length scale of the transition region, L, of 2° in longitude, and a restoring time scale, γ^{-1} = 16.7 d, which is one hundredth of the basin mode period. The hyperbolic tangent centered at 35°W results in strong restoring near the western boundary (where we have an oxygen source) and nearly zero restoring toward the eastern boundary. To ensure that tracer concentration is conserved by the model advection scheme, we followed the method used in *Marshall et al.* [2006] to correct the velocity field from the basin-mode simulation to ensure that it is horizontally nondivergent. This enables the advection term $\mathbf{u} \cdot \nabla C$ to be written in the conservative form $\nabla \cdot \left(\mathbf{u}C\right)$ used for the simulation and has only a small effect on the flow field. The velocity of the basin mode oscillations (Figure 9) was scaled such that the zonal velocity amplitude at 23°W corresponds to observed values of the EDJ cycle, which is about 10 cm s^{-1}. A standard finite difference scheme was used for the advection-diffusion model (centered in space,

leap-frog in time for the advection terms, forward in time for the diffusion term and backward in time for the consumption and restoring terms). Each model run was integrated until a steady, oscillating state was reached, that is here 36 basin-mode cycles or about 165 years.

The advection-diffusion model is aimed at studying the response of the oxygen distribution to the presence of EDJs which includes oxygen oscillations with the basin mode and changes in the mean oxygen distribution. First, we present model results of the standard configuration using the model parameters given above. The simulated mean and oscillatory response can be used to test the relevance of the EDJ cycle for the observed temporal and spatial oxygen variability.

Additionally, we present results obtained by increasing and reducing the constant oxygen consumption coefficient by a factor of five demonstrating the sensitivity of the oxygen budget and the resulting mean oxygen concentration to variations in the oxygen consumption. These simulations yield different mean zonal oxygen gradients along the equator and are used to demonstrate the sensitivity of the amplitude of oxygen oscillations to variations in the mean zonal oxygen gradient. In a last set of simulations, we included a mean zonal flow field that was constructed by using approximated meridional structures resembling the observed mean zonal velocity at 300 and 500 m along 23°W (Figure 3b, c). The zonal current bands extend all the way from the western to the eastern boundary, with the circulation closed near both boundaries. The width of the western boundary layer of the closed circulation cells was chosen such that it is smaller than the width of the oxygen restoring zone. Thus, the oxygen concentration of the water masses is relaxed to the western boundary oxygen concentration when passing through the restoring zone. The width of the eastern boundary layer was chosen to be the same as that of the western boundary layer. These additional simulations are used to discuss changes in the

oscillatory behavior of the oxygen distribution under the influence of strong ventilation of the equatorial region due to mean zonal advection.

b) Model results

In the following, we present the model results for the standard configuration (with no mean flow) in terms of oxygen concentration relative to the prescribed western boundary value. The mean relative oxygen concentration averaged over a full basin-mode cycle indicates enhanced oxygen concentration in the equatorial band away from the western boundary region (Figure 10a). The mean eastward oxygen decrease along the equator (Figure 10b) is clearly stronger than suggested by observations (relative oxygen concentration at the eastern boundary in Figure 1 is about 0.6) and likely the result of the missing ventilation due to mean eastward current bands, that are the NICC and SICC, which will be discussed further at the end of this section.

The simulated anomaly of relative oxygen at 23°W between 5°N and 5°S shows distinct patterns associated with the east- and westward propagation of Kelvin and Rossby waves, respectively (Figure 11a). Strongest anomalies are found at the equator, with the off-equatorial anomalies in general out of phase with respect to the equatorial anomalies. The simulated oxygen oscillations at 23°W are of large amplitude. They cover an oxygen range of about 60% of the total possible oxygen range (i.e., from zero to the maximum oxygen concentration at the western boundary).

The zonal velocity at 23°W is characterized by a harmonic cycle with the period of the basin mode, that is 1670 days (Figure 11b). The relative oxygen concentration instead is not harmonic; it is characterized by a relatively long period of low oxygen concentration starting before maximum westward flow is reached and a relative short period of high oxygen concentration just

after maximum eastward flow. The phase difference between the zonal velocity and the oxygen cycle is less than quadrature (i.e., phase differences of fitted harmonic cycles are smaller than 90°) resulting in a net eastward oxygen flux along the equator. This net eastward flux is the cause of the elevated oxygen concentrations in the equatorial band away from the western boundary region seen in Figure 10a.

When comparing the moored velocity and oxygen observations with the results from the advection-diffusion model (cf. Figures 6a and 11b), we note a similar phase shift between zonal velocity and oxygen associated with the EDJ cycle in observations and simulations. Observed and simulated maximum oxygen concentrations are found shortly after maximum eastward velocity. In the observations, the duration of phases with positive oxygen anomalies appears to be shorter than one half of the EDJ cycle. A similar non-harmonic behavior of the oxygen concentration can also be noted for the basin-mode simulations (cf. Figures 6a and 11b). For a more rigorous comparison, however, longer oxygen time series are required from observations.

To compare the shipboard observations with the basin mode simulations, we calculated for each ship section and the chosen depth interval the time since the last occurrence of maximum eastward flow of the EDJ cycle as obtained from the moored velocity data. Meridional structures at times corresponding to the shipboard sections (Figure 8) were then extracted from the simulations (Figure 12) and are displayed in Figure 12 with the same color coding as in Figure 8. The simulated meridional structures in the depth interval 280 to 380 m show similar variations near the equator as observed, confirming the dominant role of EDJs in shaping the equatorial oxygen distribution (cf. Figures 8a and 12a). The simulated off-equatorial lobes that are generated by Rossby wave propagation within the equatorial basin mode are barely visible in the

observations. The main reason for this difference could be the irregularity in the observations caused by meridional shifts of the mean zonal flow field, including the NICC and SEUC/SICC, and the mean oxygen distribution due to meridional motions associated with different equatorial waves such as tropical instability waves.

For the deeper depth interval 450 to 550 m, the basin-mode simulation predicts lowest oxygen concentration at the equator for the cruises in June 2006 and November 2009 which was indeed observed (cf. Figures 8b and 12b), while the model section corresponding to May/June 2011 (blue curve) is not consistent. Apart from that, the generally smaller oxygen anomalies associated with the EDJ cycle found in the observations are likely masked by other fluctuations of different space and time scales.

The sensitivity of the mean equatorial oxygen concentration to variations in the oxygen consumption coefficient is shown in Figure 10b. An increase/decrease of the oxygen consumption coefficient results in a general decrease/increase of the equatorial oxygen concentration. However, the oxygen consumption, JC, increases/decreases for an increased/decreased oxygen consumption coefficient and must be balanced by an increased/decreased oxygen flux due to the basin-mode oscillation. Within the limit $J = 0$, the oxygen concentration would reach western boundary values in the whole model domain and the oxygen flux due to the basin-mode oscillation would vanish. When considering the sensitivity of the mean oxygen flux due to the basin-mode oscillation to the oxygen consumption, it is important to remember that a balance between consumption and ventilation sets the background oxygen field, making the background oxygen field, especially its zonal gradient and its meridional and vertical curvature sensitive to the consumption. In this way consumption

influences the relative importance of processes such as mean and variable advection, lateral and vertical mixing, and wave-induced stirring in the local oxygen balance.

The simulations with increased/decreased oxygen consumption coefficient result in an increased/decreased mean zonal oxygen gradient along the equator (Figure 10b). These simulations can be used to demonstrate the sensitivity of the amplitude of oxygen oscillations to the mean zonal oxygen gradient: An increase/decrease in the mean zonal oxygen gradient is associated with an increase/decrease of oxygen fluctuations (Figure 11b). Such behavior is consistent with the observed differences in the mean zonal oxygen gradient and associated amplitude of the oxygen oscillations at 300 m and 500 m.

The simulations using a velocity field composed of a prescribed mean circulation and the basin-mode oscillation show clearly enhanced mean oxygen concentrations in the equatorial region (Figures 13 and 14). The asymmetric (Figure 13a) and symmetric (Figure 14a) mean flow fields correspond to the situations observed at 300 m (Figure 3b) and 500 m (Figure 3c) depth, respectively. Due to the increased mean oxygen concentration in the equatorial region, the amplitude of oxygen fluctuations associated with the EDJ cycle (Figures 13c and 14c) reduces strongly (roughly by a factor of 4) compared to the simulation without mean flow (Figure 11a). Without mean flow, the amplitude of oxygen fluctuations has been strongest right at the equator, which is not the case when the mean flow is included. In the latter case, similar amplitudes are found in the off-equatorial regions. In the case of the asymmetric mean flow (Figure 13), oxygen fluctuations are enhanced in the northern hemisphere compared to the southern hemisphere. In general, the amplitude of oxygen fluctuations is found to be smaller in regions of strong eastward mean flow and associated weak mean zonal oxygen gradient, that is at 4°S and 2°N (Figure 13c)

and at 2°S and 2°N (Figure 14c), respectively, compared to regions of westward or weak mean flow, which are generally characterized by stronger mean zonal oxygen gradients.

Both simulations using a mean flow show enhanced/reduced mean oxygen concentration in regions of mean eastward/westward flow. This is rather contrary to the observations showing the oxygen maximum shifted toward the equator at 300 m and a flat oxygen distribution between 2°S and 2°N at 500 m. In the simulations, the ventilation at the equator due to the EDJ cycle (Figure 10a) is not strong enough to cancel out the equatorial oxygen minimum associated with the westward mean flow (Figures 13b and 14b) and other processes have possibly to come into play to explain the observed mean meridional oxygen structure (Figure 3). Model runs using a range of values of horizontal eddy diffusivity, that is between 10 and 600 m^2 s^{-1}, (not shown) do not fundamentally change this picture – the equatorial oxygen minimum is always present. Note that the strength of the ventilation due to the mean flow depends crucially on the chosen characteristics in the western and eastern boundary layers. If the westward flow would partly recirculate before the restoring zone, the mean oxygen concentration carried by the eastward current bands would be reduced. Moreover, the mean oxygen concentration near the eastern boundary depends strongly on the eastward penetration of the eastward current bands; at present, however, there is limited knowledge from observations about the real structure of these mean circulation cells, which prevent us from using more sophisticated mean circulation pattern.

5. Summary and Discussion

Moored velocity observations taken at the equator, 23°W showed that the zonal flow beneath the EUC has significant variability associated with high vertical modes. Here, we have updated the

time series presented by *Brandt et al.* [2011], now extending over more than seven years (Figure 5). Applying a temporal harmonic fit to the zonal velocity data, we found that maximum explained variance exists on interannual time scales centered at a period of about 4.5 years (or 1670 days). These 1670-d oscillations are found to be a characteristic of EDJs in the Atlantic Ocean having a vertical wavelength of about 400 m and downward phase propagation [*Johnson and Zhang*, 2003; *Bunge et al.*, 2008; *Brandt et al.*, 2011]. *Greatbatch et al.* [2012] used a reduced-gravity model to simulate an equatorial basin mode for a high-order baroclinic mode. In the present study an advection-diffusion model was forced by the velocity field of this basin-mode model to study the effect of EDJ oscillations on the oxygen distribution at intermediate depths. The advection-diffusion model includes restoring to high oxygen values at the western boundary and oxygen consumption elsewhere. In the absence of mean flow, the advection-diffusion model predicts 1) a phase shift between maximum eastward velocity and oxygen concentration within the EDJ cycle, 2) elevated oxygen variability at the equator compared to the off-equatorial variability, and 3) a weak net ventilation of the equatorial band by EDJs.

Through the comparison of the basin-mode simulation with the available moored and shipboard data at intermediate depths below the EUC, we conclude that 1) a substantial part of the observed oxygen variability at the equator is due to EDJ oscillations, 2) oxygen fluctuations at the equator are weaker at depths with reduced mean zonal oxygen gradient such as at 500 m compared to depth intervals with increased zonal oxygen gradient such as at 300 m, and 3) the phase shift between maximum zonal velocity and maximum oxygen concentration is less than quadrature implying a mean eastward oxygen flux due to EDJs.

The mean oxygen distribution in the equatorial Atlantic, with high oxygen concentration in the

western and low oxygen concentration in the eastern basin can to first order be explained by ventilation due to the energetic western boundary current system governed by the equator-crossing, oxygen-rich NBC [*Schott et al.*, 2005] and oxygen consumption elsewhere. The mean eastward flow of the NICC and SICC has been identified as the main ventilation pathway toward the oxygen minimum zones of the eastern equatorial Atlantic [*Tsuchiya et al.*, 1992; *Schott et al.*, 1998; *Stramma et al.*, 2005], which is here confirmed by the simulations presented in section 4 that are forced by a mean zonal velocity field superimposed on the gravest equatorial basin mode. The simulated eastward advection of oxygen-rich waters by the mean flow field resulted in a strong increase of the oxygen levels in the equatorial region compared to the simulation without mean flow. Note that in our simulations the strength of the ventilation by the mean flow is likely overestimated. Model simulations [*Hüttl-Kabus and Böning*, 2008] as well as shipboard velocity sections [*Fischer et al.*, 2008] have shown that the SEUC is partly supplied by recirculation of (lower-oxygen) waters out of westward current branches. In the observations, the SEUC doubles in strength from the western boundary at 35°W toward the middle of the basin. Such recirculation that is not connected to high-oxygen levels at the western boundary is also likely for the NICC and SICC but less covered by observations or reproduced by simulations.

Phases of eastward EDJ flow lead as well to eastward advection of oxygen-rich waters from the western boundary. The quantification of the EDJ influence on the mean meridional oxygen structure from observations (Figure 3) is difficult, given the limited length of available time series. Qualitatively, the ventilation mechanism can be described as follows: EDJ oscillations generate narrow oxygen tongues with strong meridional oxygen gradients. These tongues are mainly eroded by meridional diffusion along their zonal extent [*Brandt et al.*, 2008] such that

zonal velocity and oxygen oscillations are less than quadrature which implies a net eastward oxygen flux. However, the presented basin-mode simulations including mean advection still show a local oxygen minimum at the equator in the meridional oxygen distributions (Figures 13b and 14b) which is not present in the observations (Figure 3). Thus, other processes might contribute to enhance the oxygen concentration at the equator compared to the off-equatorial regions such as, for instance, vertical mixing below the EUC. However, the vertical mixing at the equator below the EUC shear zone was suggested to be substantially smaller than at mid-latitudes [*Gregg et al.*, 2003]. By analyzing the vertical and meridional oxygen curvature of an oxygen tongue generated by an eastward jet at the equator, *Brandt et al.* [2008] have estimated the effect of vertical oxygen diffusion for eroding the observed oxygen tongue during its eastward progression and found it an order of magnitude smaller than the effect of lateral eddy diffusion. Nevertheless, the curvature of the mean vertical oxygen profile (Figure 4) suggests a possible contribution of vertical mixing to the ventilation at 300 m depth, but not at 500 m depth. At 500 m depth, the curvature is strongly reduced or even reversed indicating rather a local reduction of the oxygen concentration due to vertical diffusion. A ventilation mechanism acting right at the equator that was suggested by *Li et al.* [1996] is wave-induced stirring. By using a reduced-gravity model, they could show that the combination of annual Rossby waves and intraseasonal mixed Rossby-gravity waves results in an eastward tracer transport. Such interaction and/or the combination of the equatorial basin mode and intraseasonal mixed Rossby-gravity waves could contribute to explain the identified differences between simulated and observed meridional oxygen structures. Another possible explanation is that the Stokes drift associated with velocity fluctuations near the equator plays a role in setting the mean oxygen

distribution. As noted by *Moore* [1970] and *Ascani et al.* [2010], the Stokes drift can be expected to oppose the Eulerian mean flow, weakening the influence of the mean flow that is seen in Figures 13 and 14 - a topic for future investigation.

Up to now, state-of-the-art coarse-resolution simulations fail to adequately reproduce the oxygen distribution in the tropical oceans. High levels of numerically induced diapycnal mixing in such models have been suggested to be responsible for the model limitations [*Keeling et al.*, 2010]. Furthermore, *Duteil and Oschlies* [2011] showed only small improvements in the simulated oxygen distribution when running coarse-resolution models with more realistic levels of diapycnal mixing. However, these models lack realistic zonal advection by narrow mean equatorial and off-equatorial jets and EDJs. The equatorial oxygen maximum – a characteristic of the observed mean oxygen distribution in the tropical oceans – and associated ventilation of the oxygen minimum zones by poleward eddy fluxes is in fact strongly underestimated in these simulations [*Meissner et al.*, 2005]. Recent high-resolution ocean process model studies start to capture the dynamics of the mean equatorial and off-equatorial jets and/or EDJs [*d'Orgeville et al.*, 2007; *Hua et al.*, 2008; *Eden and Dengler*, 2008; *Ménesguen et al.*, 2009; *Ascani et al.*, 2010]. These process simulations provide the dynamic background for improving equatorial ocean oxygen distributions in physical-biogeochemical models, either by suggesting ways to include the missing dynamics or to parameterize these flow features.

Appendix A: Data

a) Moored observations

In this study, we use mooring data from five successive deployment periods at the equator, 23°W

of nearly 1.5 years each. The total timeframe covers the period from February 2004 to June 2011. During these deployment periods, the mooring was equipped with two ADCPs, the upper one looking upward from just below the EUC, typically at 100 to 150 m depth, while the lower one looked either downward from beneath the upper instrument or upward from about 600 to 650 m depth. The upper instrument failed during two deployment periods which, however, does not affect the present study as the depth interval of interest here was completely covered by the deeper instrument. We applied a 40-h low-pass filter to hourly-interpolated current data (ADCP sampling rates varied typically between 0.5 and 1 per hour, but it was set to about 3 per day during one mooring period) to eliminate tidal currents and the detided data were subsequently subsampled to 12-hourly resolution.

The moored data were used to calculate the mean profile of the zonal velocity and the standard error of the mean. The standard error was obtained by dividing the standard deviation by the square root of the number of degrees of freedom. The number of degrees of freedom was estimated as the length of the available time series divided by a quarter of the EDJ cycle.

Following *Brandt et al.* [2011], harmonic analyses of moored zonal velocities were performed by fitting the following linear regression model in a least-squares sense to the data. The model fit is given by

$$d_m = g \cdot \beta = \beta_1 + \beta_2 \cdot \cos(\omega t) + \beta_3 \cdot \sin(\omega t), \qquad \text{(A1)}$$

with time vector t, $\omega = 2\pi / p$, where p is the period, model matrix g, and column vector β containing the model factors $\beta_1, \beta_2, \beta_3$. The error matrix is given by

$$\Delta\beta = \sqrt{\frac{\left(g^T \cdot g\right)^{-1} \cdot \left(\left(d - d_m\right)^T \cdot \left(d - d_m\right)\right)}{n - k}}, \qquad \text{(A2)}$$

with data vector d, degrees of freedom n, and number of dependent model factors k = 2. The standard errors of the elements of β are given by the diagonal elements of $\Delta\beta$. After subtracting the mean seasonal cycle, the moored zonal velocity data were 270-d low-pass filtered and 0.5-year subsampled. The corresponding number of degrees of freedom was estimated as the length of the available time series divided by a quarter of the EDJ cycle.

During the last two mooring periods, the mooring was equipped with regular Seabird MicroCAT temperature/salinity probes and Aanderaa oxygen optodes at 300 and 500 m depth. During the first deployment period, the oxygen probes equipped with optodes of type 3830 failed because of too high power consumption of the data loggers and we obtained only 16 days of oxygen data. The second deployment, with an optode of type 4330 at 300 m and of type 3830 at 500 m, however, delivered complete datasets. The optode measurements were calibrated as follows: The oxygen probes were attached to the rosette during regular CTD/O_2 casts before and after the mooring deployment, with the shipboard oxygen measurements being calibrated against oxygen concentrations from Winkler titrations of water samples throughout the cruises. Additionally, on-board optode measurements were performed in water baths with zero and saturated oxygen concentrations. Finally, the phase signals from the optode output were calibrated against the oxygen concentrations of the calibrated CTD/O_2 measurements and the zero-oxygen concentration of the water bath following *Uchida et al.* [2008]. A fixed salinity dependence after *Garcia and Gordon* [1992] was applied subsequently. From the misfit of the calibration and by comparing pre- and post-calibration, we estimated the error of the moored dissolved oxygen

measurements to be smaller than 3 μmol kg^{-1}.

b) Shipboard measurements

Shipboard hydrographic and current measurements obtained from various research cruises in the central tropical Atlantic during 1996-2011 are utilized. For the mean fields, we use data acquired between 22° and 24°W from the data base described in *Brandt et al.* [2010] with two additional cruises performed in October/November 2009 (RV Meteor 80/1) and in May/June 2011 (RV Maria S. Merian 18/2). To study the temporal and spatial variability of the oxygen concentrations along 23°W, we analyze data of four particular cruises comprising the above most recent cruises as well as two earlier cruises in June/July 2006 (RV Meteor 68/2) and in February/March 2008 (RV L'Atalante IFM-GEOMAR-4). The obtained data accuracy is similar to the standards set by the World Ocean Circulation Experiment which is about 1% for dissolved oxygen concentration.

From the ship sections, mean velocity and oxygen concentration fields were calculated as described in detail by *Brandt et al.* [2010]. The standard error of the mean was here derived by estimating the number of degrees of freedom from the number of available shipboard measurements at each grid point.

Acknowledgments. This study was supported by the German Science Foundation as part of the Sonderforschungsbereich 754 "Climate-Biogeochemistry Interactions in the Tropical Ocean" and by the German Federal Ministry of Education and Research as part of the co-operative project "North Atlantic". Moored velocity observations were acquired in cooperation with the PIRATA project. The authors thank Marcus Dengler, François Ascani, and John Toole for helpful discussions, Yao Fu for help with the reduced-gravity model, and three anonymous reviewers for

their helpful comments.

References

Ascani, F., E. Firing, P. Dutrieux, J. P. McCreary, and A. Ishida (2010), Deep equatorial ocean circulation induced by a forced-dissipated Yanai beam, *J. Phys. Oceanogr.*, *40*, 1118-1142, doi:10.1175/2010JPO4356.1.

Bourlès, B., C. Andrié, Y. Gouriou, G. Eldin, Y. du Penhoat, S. Freudenthal, B. Dewitte, F. Gallois, R. Chuchla, F. Baurand, A. Aman, and G. Kouadio (2003), The deep currents in the Eastern Equatorial Atlantic Ocean, *Geophys. Res. Lett.*, *30*, 8002, doi:10.1029/2002GL015095.

Brandt, P., F. A. Schott, C. Provost, A. Kartavtseff, V. Hormann, B. Bourlès, and J. Fischer (2006), Circulation in the central equatorial Atlantic: Mean and intraseasonal to seasonal variability, *Geophys. Res. Lett.*, 33, L07609, doi:10.1029/2005GL025498.

Brandt, P., V. Hormann, B. Bourlès, J. Fischer, F. A. Schott, L. Stramma, and M. Dengler (2008), Oxygen tongues and zonal currents in the equatorial Atlantic, *J. Geophys. Res.*, *113*, C04012, doi:10.1029/2007JC004435.

Brandt, P., V. Hormann, A. Körtzinger, M. Visbeck, G. Krahmann, L. Stramma, R. Lumpkin, and C. Schmid (2010), Changes in the ventilation of the oxygen minimum zone of the tropical North Atlantic, *J. Phys. Oceanogr.*, *40*, 1784–1801, doi: 10.1175/2010JPO4301.1.

Brandt, P., A. Funk, V. Hormann, M. Dengler, R. J. Greatbatch, and J. M. Toole (2011), Interannual atmospheric variability forced by the deep equatorial Atlantic Ocean, *Nature*, 473, 497-500, doi:10.1038/nature10013.

Bunge, L., C. Provost, B. L. Hua, and A. Kartavtseff (2008), Variability at intermediate depths at the equator in the Atlantic Ocean in 2000–06: Annual cycle, equatorial deep jets, and intraseasonal meridional velocity fluctuations, *J. Phys. Oceanogr.*, *38*, 1794–1806, doi:10.1175/2008JPO3781.1.

Cane, M. A., and D. W. Moore (1981), A note on low-frequency equatorial basin modes, *J. Phys. Oceanogr.*, 11, 1578–1584.

d'Orgeville, M., B. L. Hua, and H. Sasaki (2007), Equatorial deep jets triggered by a large vertical scale variability within the western boundary layer, *J. Mar. Res.*, 65, 1-25.

Duteil, O., and A. Oschlies (2011), Sensitivity of simulated extent and future evolution of marine suboxia to mixing intensity, *Geophys. Res. Lett.*, 38, L06607, doi:10.1029/2011GL046877.

Eden, C., and M. Dengler (2008), Stacked jets in the deep equatorial Atlantic Ocean, *J. Geophys. Res.*, 113, C04003, doi:10.1029/2007JC004298.

Fischer, J., V. Hormann, P. Brandt, F. A. Schott, B. Rabe, and A. Funk (2008), South Equatorial Undercurrent in the western to central tropical Atlantic, *Geophys. Res. Lett.*, 35, L21601, doi:101029/2008GL035753.

Garcia, H. E., and L. I. Gordon (1992), Oxygen solubility in seawater: Better fitting equations, *Limnology and Oceanography*, 37, 1307-1312.

Garcia, H. E., T. P. Boyer, S. Levitus, R. A. Locarnini, and J. Antonov (2005), On the variability of dissolved oxygen and apparent oxygen utilization content for the upper world ocean: 1955 to 1998, *Geophys. Res. Lett.*, 32, L09604, doi:10.1029/2004GL022286.

Gouretski, V. V., and K. P. Koltermann (2004), WOCE Global Hydrographic Climatology [CD-ROM], *Rep. 35*, 52 pp., Bundesamt für Seeschifffahrt und Hydrographie, Hamburg, Germany.

Gouriou, Y., C. Andrié, B. Bourlès, S. Freudenthal, S. Arnault, A. Aman, G. Eldin, Y. du Penhoat, F. Baurand, F. Gallois, and R. Chuchla (2001), Deep circulation in the equatorial Atlantic Ocean, *Geophys. Res. Lett.*, 28(5), 819–822, doi:10.1029/2000GL012326.

Greatbatch, R. J., P. Brandt, M. Claus, S.-H. Didwischus, and Y. Fu (2012), On the width of the equatorial deep jets, *J. Phys. Oceanogr.*, 42, 1729–1740, doi:10.1175/JPO-D-11-0238.1.

Gregg, M. C., T. B. Sanford, and D. P. Winkel (2003), Reduced mixing from the breaking of internal waves in equatorial ocean waters, *Nature*, 422, 513–515.

Hua B. L., M. d'Orgeville, M. D. Fruman, C. Menesguen, R. Schopp, P. Klein, and H. Sasaki (2008), Destabilization of mixed Rossby gravity waves and the formation of equatorial zonal jets, *J. Fluid Mech.*, 610, 311-341.

Hüttl-Kabus, S., and C. W. Böning (2008), Pathways and variability of the off-equatorial undercurrents in the Atlantic Ocean, *J. Geophys. Res.*, 113, C10018, doi:10.1029/2007JC004700.

Johnson, G. C., and D. Zhang (2003), Structure of the Atlantic Ocean equatorial deep jets, *J. Phys. Oceanogr., 33*, 600-609.

Johnson, G. C., and N. Gruber (2007), Decadal water mass variations along 20°W in the Northeastern Atlantic Ocean, *Progress in Oceanography*, 73, 277–295.

Johnson, G. C., E. Kunze, K. E. McTaggart, and D. W. Moore (2002), Temporal and spatial structure of the equatorial deep jets in the Pacific Ocean, *J. Phys. Oceanogr.*, 32, 3397-3407.

Karstensen, J., L. Stramma, and M. Visbeck (2008), The oxygen minimum zones in the eastern tropical Atlantic and Pacific oceans, *Progress in Oceanography*, 77, 331-350, doi:10.1016/j.pocean.2007.05.009.

Keeling, R. F., A. Körtzinger, and N. Gruber (2010), Ocean deoxygenation in a warming world, *Ann. Rev. Mar. Sci*, 2, 199-229.

Li, X., P. Chang, and R. C. Pacanowski (1996), A wave-induced stirring mechanism in the mid-depth equatorial ocean, *J. Mar. Res.*, 54, 487-520.

Luyten, J. R., and J. C. Swallow (1976), Equatorial undercurrents, *Deep-Sea Res.*, 23, 999-1001.

Marshall, J., E. Shuckburgh, H. Jones, and C. Hill (2006), Estimates and implications of surface eddy diffusivity in the Southern Ocean derived from tracer transport, *J. Phys. Oceanogr.*, 36, 1806–1821, doi:10.1175/JPO2949.1.

Meissner, K. J., E. D. Galbraith, and C. Volker (2005), Denitrification under glacial and interglacial conditions: A physical approach, *Paleoceanography*, 20, PA3001, doi:10.1029/2004PA001083.

Ménesguen, C., B. L. Hua, M. Fruman, and R. Schopp (2009), Dynamics of the combined extra-equatorial and equatorial deep jets in the Atlantic, *J. Mar. Res.*, 67, 323-346, doi: 10.1357/002224009789954766.

Moore, D. W. (1970), The mass transport velocity induced by free oscillations at a single frequency, *Geophys. Fluid Dyn.*, 1, 237-247.

Ponte, R. M., and J. R. Luyten (1990), Deep velocity measurements in the western equatorial Indian Ocean, *J. Phys. Oceanogr.*, *20*, 44-52.

Schott, F. A., J. Fischer, and L. Stramma (1998), Transports and pathways of the upper-layer circulation in the western tropical Atlantic, *J. Phys. Oceanogr.*, *28*, 1904–1928.

Schott, F., M. Dengler, R. J. Zantopp, L. Stramma, J. Fischer, and P. Brandt (2005), The shallow and deep western boundary circulation of the South Atlantic at 5°–11°S, *J. Phys. Oceanogr.*, *35*, 2031-2053.

Stramma, L., S. Hüttl, and J. Schafstall (2005), Water masses and currents in the upper tropical northeast Atlantic off northwest Africa, *J. Geophys. Res.*, 110, C12006, doi:10.1029/2005JC002939.

Stramma, L., G. C. Johnson, J. Sprintall, and V. Mohrholz (2008), Expanding oxygen minimum zones in the tropical oceans, *Science*, 320, 655–658.

Tsuchiya, M., L. D. Talley, and M. S. McCartney (1992), An eastern Atlantic section from Iceland southward across the equator, *Deep Sea Res.*, *39*, 1885–1917.

Uchida, H., T. Kawano, I. Kaneko, and M. Fukasawa (2008), In situ calibration of optode-based oxygen sensors, *J. Atmos. Oceanic Technol.*, 25, 2271–2281.

van Geen, A., W. M. Smethie Jr., A. Horneman, and H. Lee (2006), Sensitivity of the North Pacific oxygen minimum zone to changes in ocean circulation: A simple model calibrated by chlorofluorocarbons, *J. Geophys. Res.*, 111, C10004, doi:10.1029/2005JC003192.

Wattenberg H. (1939), Die Verteilung des Sauerstoffs im Atlantischen Ozean, Deutsche Atlantische Expedition Meteor 1925–1927, Wiss. Erg., Bd. 9, 132 pp.

Whitney, F.A., Freeland, H.J., and Robert, M. (2007), Persistently declining oxygen levels in the interior waters of the eastern subarctic Pacific, *Progress in Oceanography*, 75, 179–199.

Figure 1. Climatological distribution of the oxygen concentration [μmol kg^{-1}] at 300-500 m in the tropical Atlantic [*Gouretski and Koltermann*, 2004], with superimposed repeat ship section along the 23°W meridian (thick white line) and the equatorial mooring position (diamond). Also included are major thermocline (black solid arrows) and intermediate (black dashed arrows) current branches: North Brazil Current (NBC), North and South Equatorial Undercurrent (NEUC, SEUC), and Equatorial Undercurrent (EUC), as well as Southern and Northern Intermediate Countercurrents (NICC, SICC), and Equatorial Intermediate Current (EIC).

Figure 2. Mean zonal velocity (a) and oxygen concentration (b) along 23°W from ship sections (update from *Brandt et al.* [2010]). Thick black solid lines mark surfaces of uniform potential density. In (a), negative values indicating westward flow are shown by dashed contours and the contour interval is 5 cm s^{-1} within the range from −10 cm s^{-1} to 10 cm s^{-1} and 10 cm s^{-1} elsewhere.

Figure 3. Mean meridional structure of observed zonal velocity (red, left axis) and oxygen (black, right axis) along 23°W at 150 m (a), 300 m (b), and 500 m (c), with standard errors of the mean (dashed).

Figure 4. Mean equatorial profiles of observed zonal velocity (red, upper axis) and oxygen (black, lower axis) at 23°W, with standard error of the mean (dashed). The zonal velocity profile

was obtained from more than seven years of moored observations (Figure 5). The oxygen profile is taken from the mean shipboard section (Figure 2b). The red dotted line marks zero velocity.

Figure 5. Zonal velocity from moored observations at the equator, 23°W, with superimposed phase lines obtained from a harmonic analysis using a period of 1670 days (solid: maximum eastward velocity, dashed: maximum westward velocity).

Figure 6. Zonal velocity from moored observations at the equator, 23°W, with overlaid 1670-d harmonic fit (red, left axis) and oxygen concentration from moored instruments (black, right axis) at 300 m (a) and 500 m (b) depth. The mean oxygen concentration at 300 m and 500 m depth from ship sections is 103±5 μmol kg^{-1} and 129±3 μmol kg^{-1} (thick black dashed lines), respectively, with standard errors marked by thin black dashed lines. Note that the oxygen range in (a) is twice as large as in (b).

Figure 7. Oxygen distributions along 23°W taken during research cruises in June 2006 (a), February/March 2008 (b), November 2009 (c), and May/June 2011 (d).

Figure 8. Observed meridional oxygen structure along 23°W. Shipboard measurements taken during research cruises in June 2006 (black), February/March 2008 (red), November 2009

(green), and May/June 2011 (blue) were averaged between 280 and 380 m depth (a), and between 450 and 550 m depth (b).

Figure 9. Amplitude (a) and phase (b) of the zonal velocity associated with an equatorial basin mode for a high-order baroclinic mode (gravity wave speed c = 0.17 m s^{-1}) using a lateral eddy viscosity of 200 m^2 s^{-1} as simulated by the reduced-gravity model of *Greatbatch et al.* [2012] after subtracting the divergent part of the velocity field (see the text for details). The amplitude is normalized by the maximum zonal velocity amplitude. In (b), solid contours show positive phase, indicating a lag compared to zero, and dashed contours show negative phase. The contour interval is 45°.

Figure 10. Horizontal map (a) and equatorial distribution (b) of the simulated mean relative oxygen concentration averaged over a full basin-mode cycle. Note that oxygen is normalized relative to the value used for the restoring at the western boundary. In (b), simulations with the oxygen consumption coefficient increased (dashed)/decreased (dotted) by a factor of five are also included.

Figure 11. Simulated anomaly of relative oxygen at 23°W for a full basin mode cycle, T_0 = 1670 d, (a) as a function of latitude and time (in parts of the cycle) and (b) only at the equator (black, right axis). The zonal velocity used to force the advection-diffusion model is included in (b) (red, left axis). The simulation started after a model spin-up of 36 basin-mode cycles to ensure a

steady, oscillating oxygen distribution. In (a), negative values are shown by dashed contours and the contour interval is 0.1. In (b), simulations with the oxygen consumption coefficient increased (dashed)/decreased (dotted) by a factor of five are also included.

Figure 12. Simulated meridional oxygen structure along 23°W. Simulations are extracted corresponding to the measurements shown in Figure 8 in the depth interval 280 to 380 m (a) at 263 days (black), 884 days (red), 1505 days (green), and 403 days (blue) and in the depth interval 450 to 550 m (b) at 1136 days (black), 87 days (red), 708 days (green), and 1276 days (blue) after maximum eastward velocity of the basin-mode cycle at the equator, 23°W.

Figure 13. Horizontal maps of (a) the prescribed mean zonal velocity and (b) the simulated mean relative oxygen concentration averaged over a full basin-mode cycle. The simulated anomaly of relative oxygen at 23°W for a full basin-mode cycle, T_0 = 1670 d, is shown in (c) as a function of latitude and time (in parts of the cycle) and the equatorial distribution of the simulated mean relative oxygen concentration averaged over a full basin-mode cycle is presented in (d). The mean zonal velocity field used in this simulation corresponds to the observed zonal velocity at 300 m depth (cf. Figure 3b).

Figure 14. Same as Figure 13, but the mean zonal velocity field used in this simulation corresponds to the observed zonal velocity at 500 m depth (cf. Figure 3c).

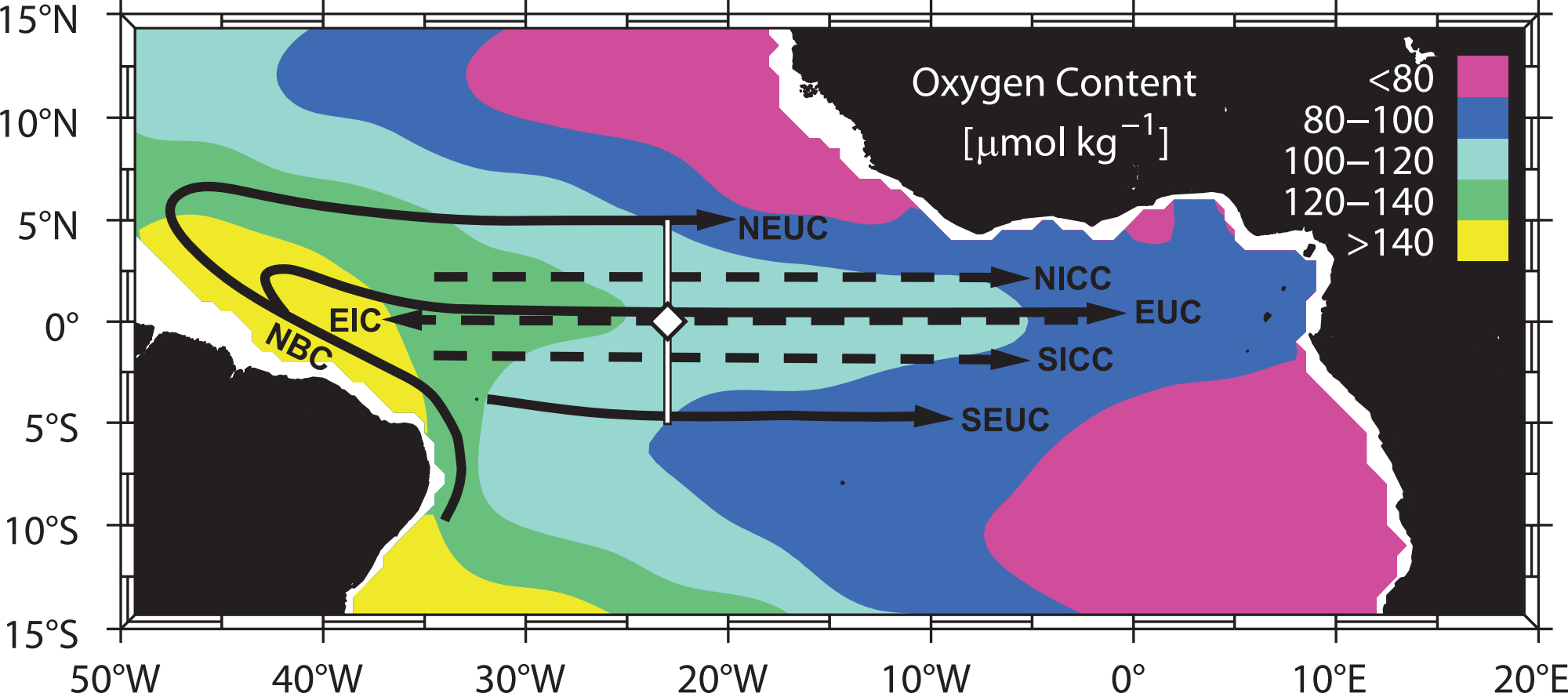
Oxygen Content
[μmol kg^{-1}]
<80
80–100
100–120
120–140
>140
NEUC
NICC
EUC
SICC
SEUC
EIC
NBC
15°N
10°N
5°N
0°
5°S
10°S
15°S
50°W
40°W
30°W
20°W
10°W
0°
10°E
20°E

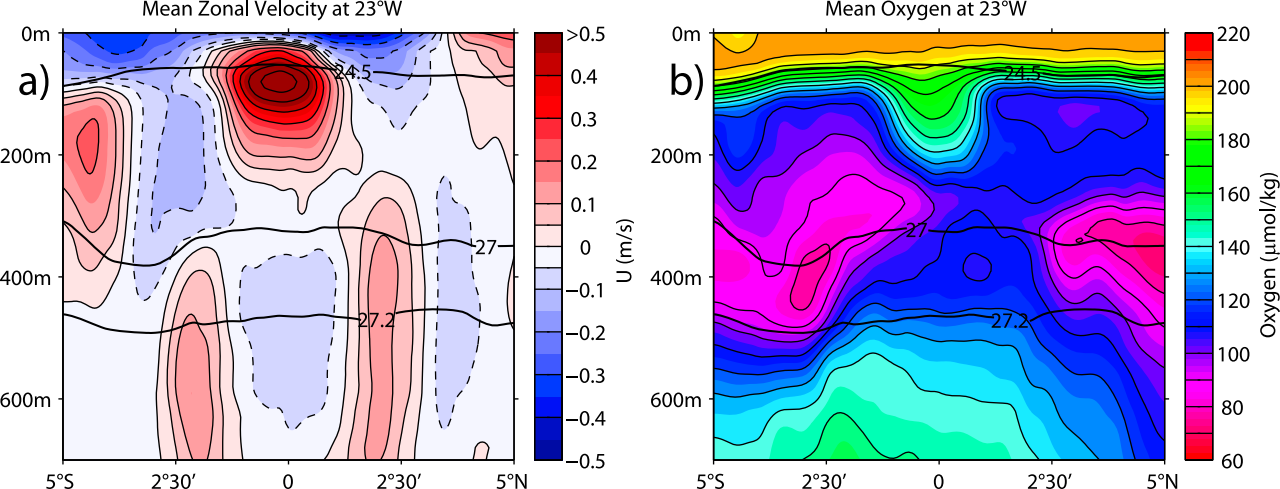
Mean Zonal Velocity at 23°W
a)
0m
200m
400m
600m
24.5
27
27.2
5°S
2°30′
0
2°30′
5°N
>0.5
0.4
0.3
0.2
0.1
0
−0.1
−0.2
−0.3
−0.4
−0.5
U (m/s)
Mean Oxygen at 23°W
b)
0m
200m
400m
600m
24.5
27
27.2
5°S
2°30′
0
2°30′
5°N
220
200
180
160
140
120
100
80
60
Oxygen (µmol/kg)

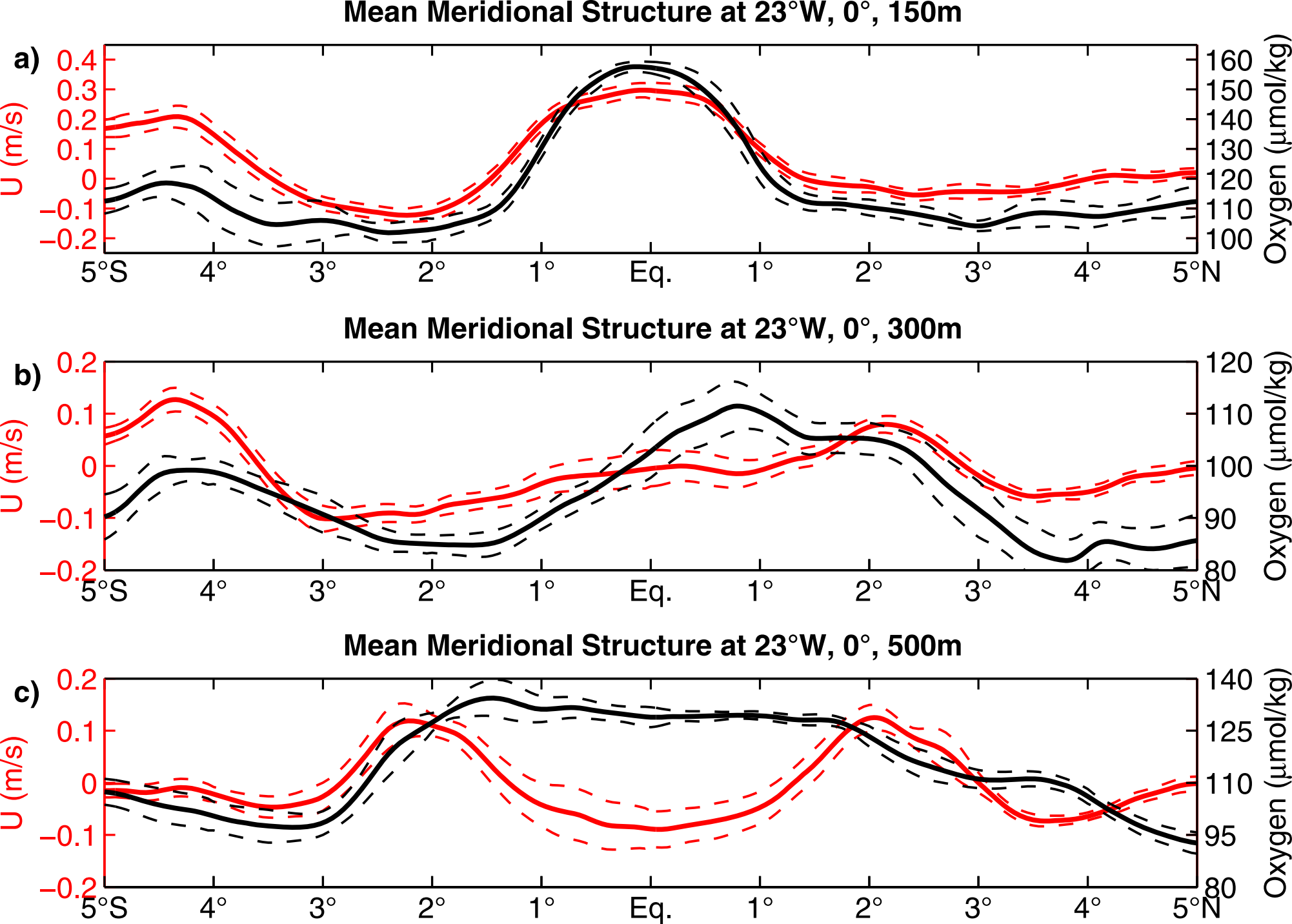
Mean Meridional Structure at 23°W, 0°, 150m
a)
U (m/s)
Oxygen (µmol/kg)
0.4
0.3
0.2
0.1
0
−0.1
−0.2
160
150
140
130
120
110
100
5°S
4°
3°
2°
1°
Eq.
1°
2°
3°
4°
5°N
Mean Meridional Structure at 23°W, 0°, 300m
b)
U (m/s)
Oxygen (µmol/kg)
0.2
0.1
0
−0.1
−0.2
120
110
100
90
80
5°S
4°
3°
2°
1°
Eq.
1°
2°
3°
4°
5°N
Mean Meridional Structure at 23°W, 0°, 500m
c)
U (m/s)
Oxygen (µmol/kg)
0.2
0.1
0
−0.1
−0.2
140
125
110
95
80
5°S
4°
3°
2°
1°
Eq.
1°
2°
3°
4°
5°N

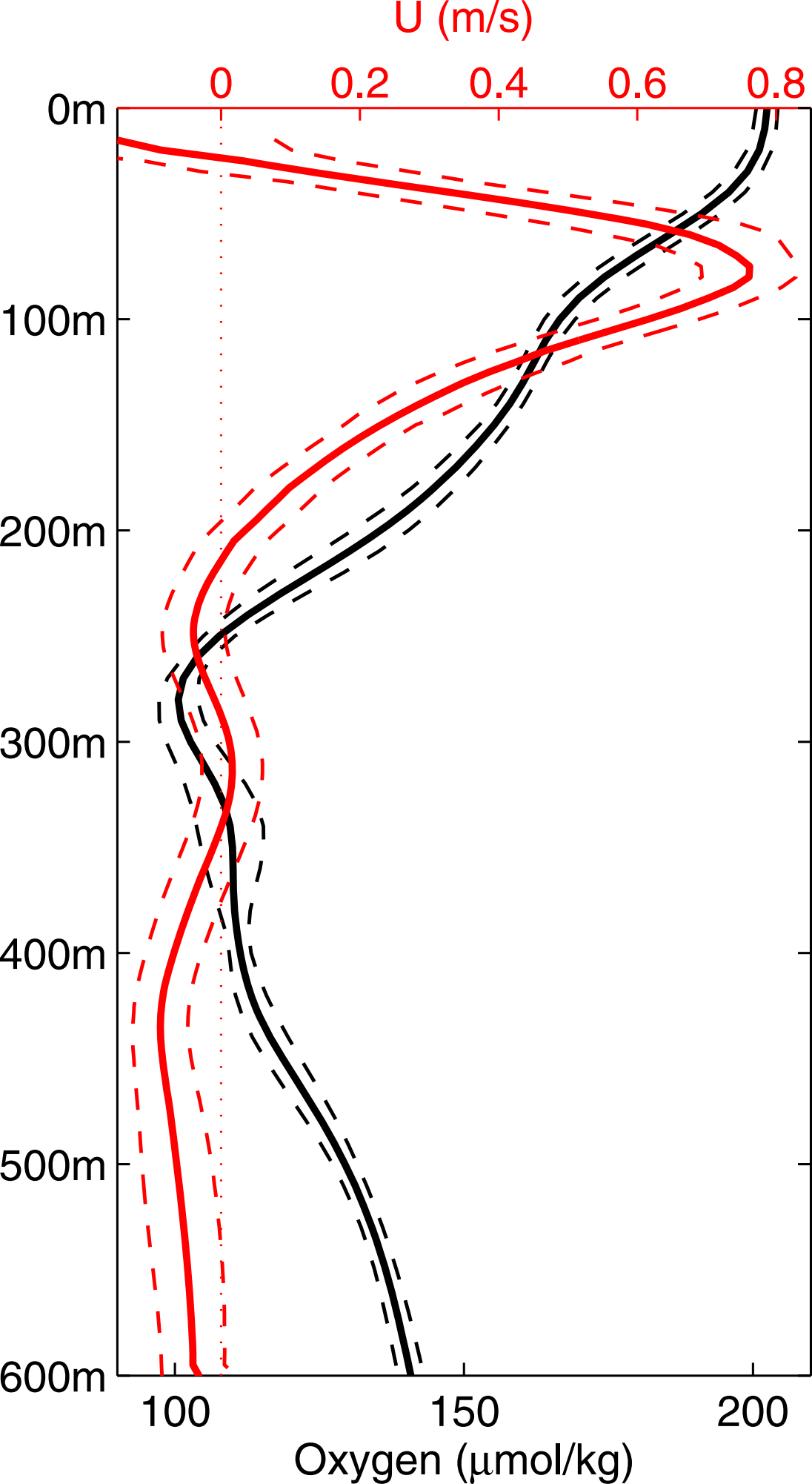
U (m/s)
0
0.2
0.4
0.6
0.8
0m
100m
200m
300m
400m
500m
600m
100
150
200
Oxygen (µmol/kg)

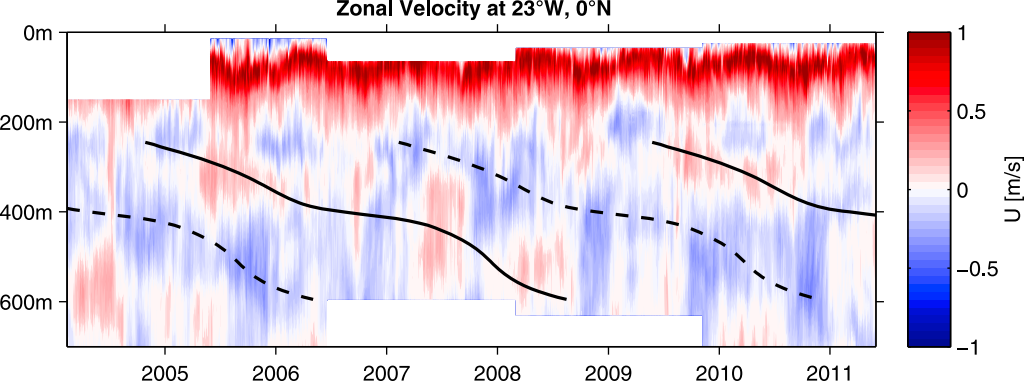
Zonal Velocity at 23°W, 0°N
0m
200m
400m
600m
2005
2006
2007
2008
2009
2010
2011
1
0.5
0
−0.5
−1
U [m/s]

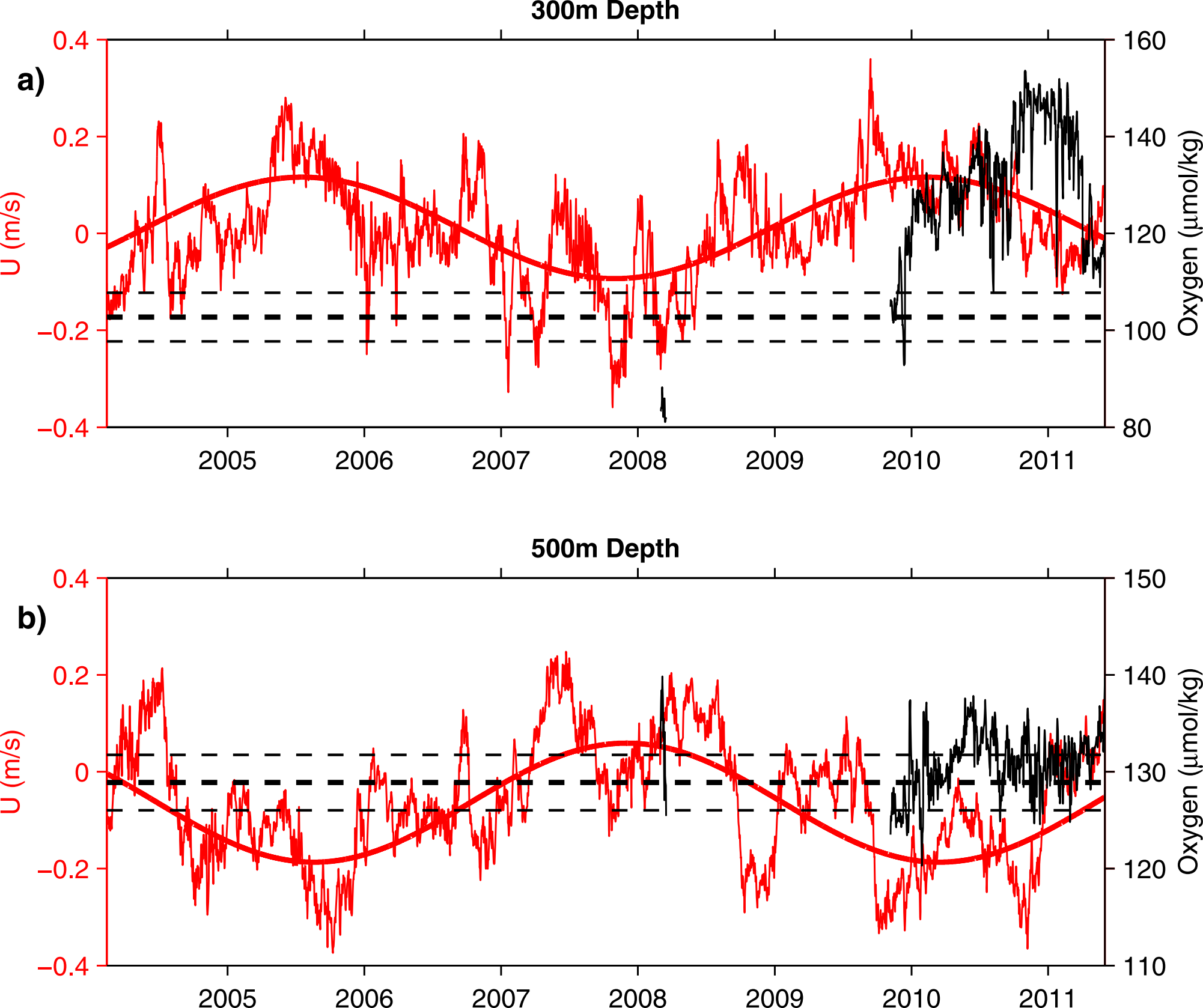
300m Depth
a)
0.4
0.2
0
−0.2
−0.4
U (m/s)
160
140
120
100
80
Oxygen (µmol/kg)
2005
2006
2007
2008
2009
2010
2011
500m Depth
b)
0.4
0.2
0
−0.2
−0.4
U (m/s)
150
140
130
120
110
Oxygen (µmol/kg)
2005
2006
2007
2008
2009
2010
2011

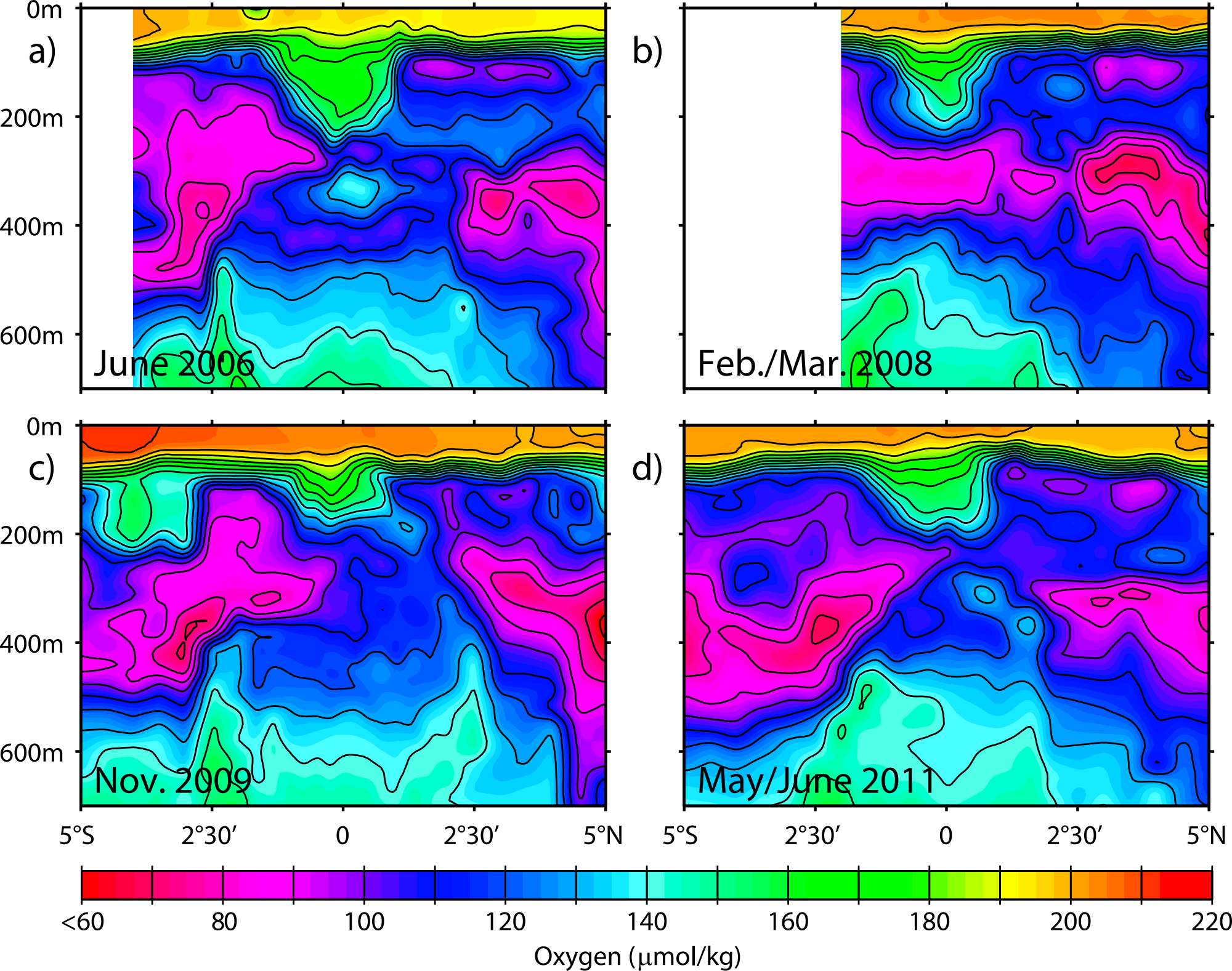
a)
b)
c)
d)
0m
200m
400m
600m
June 2006
Feb./Mar. 2008
Nov. 2009
May/June 2011
5°S
2°30′
0
2°30′
5°N
<60
80
100
120
140
160
180
200
220
Oxygen (µmol/kg)

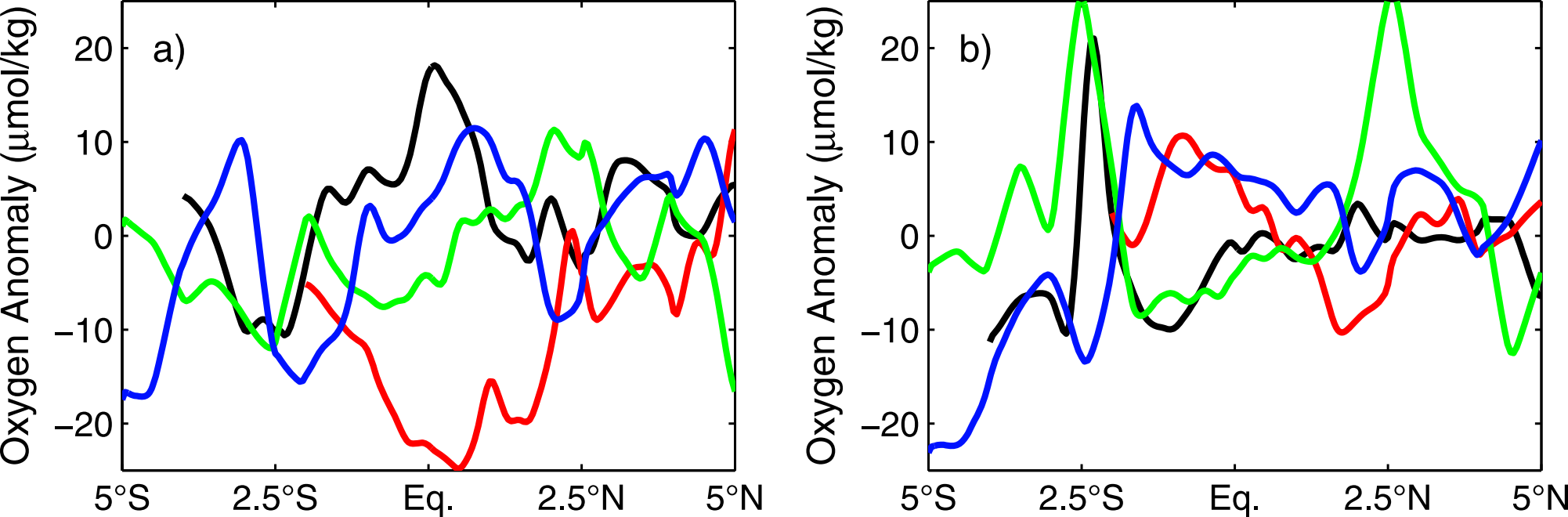
a)
b)
Oxygen Anomaly (µmol/kg)
20
10
0
−10
−20
5°S
2.5°S
Eq.
2.5°N
5°N

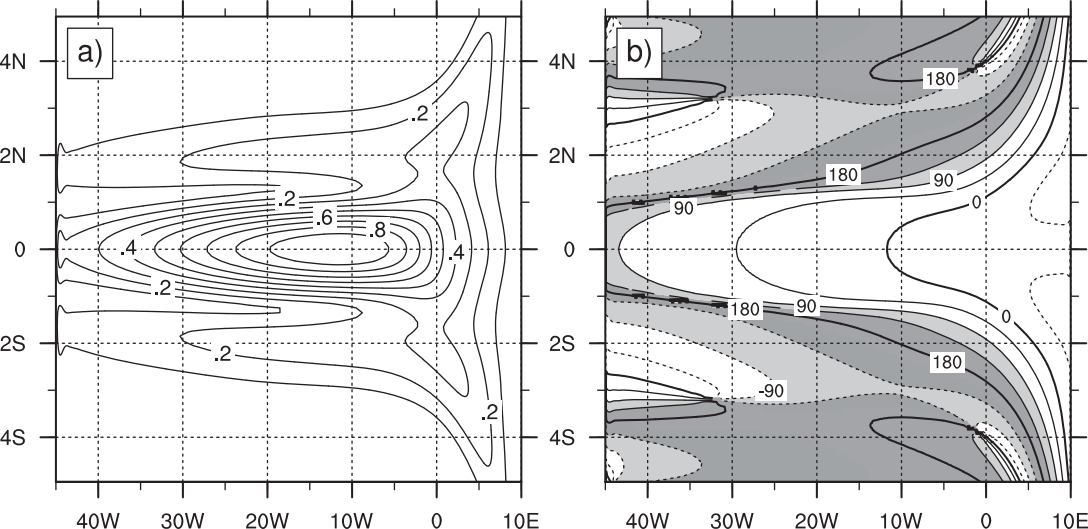
a)
b)
4N
2N
0
2S
4S
40W
30W
20W
10W
0
10E
.2
.4
.6
.8
180
90
-90

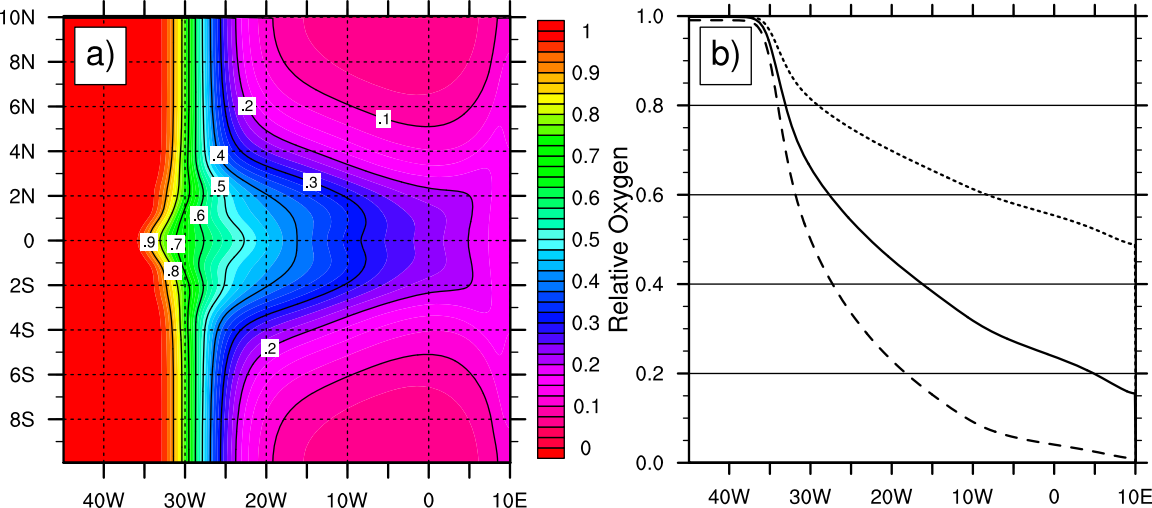
a)
b)
10N
8N
6N
4N
2N
0
2S
4S
6S
8S
40W
30W
20W
10W
0
10E
.1
.2
.3
.4
.5
.6
.7
.8
.9
.2
1
0.9
0.8
0.7
0.6
0.5
0.4
0.3
0.2
0.1
0
Relative Oxygen
1.0
0.8
0.6
0.4
0.2
0.0

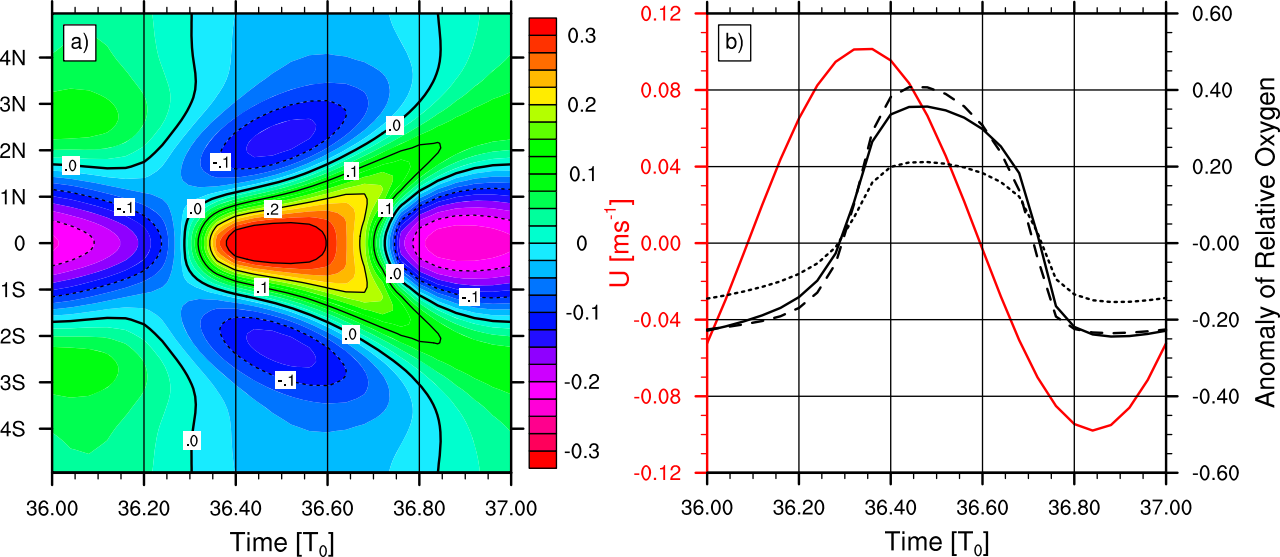
a)
b)
4N
3N
2N
1N
0
1S
2S
3S
4S
.0
-.1
.1
.2
0.3
0.2
0.1
0
-0.1
-0.2
-0.3
36.00
36.20
36.40
36.60
36.80
37.00
Time [T0]
0.12
0.08
0.04
0.00
-0.04
-0.08
-0.12
U [ms-1]
0.60
0.40
0.20
-0.00
-0.20
-0.40
-0.60
Anomaly of Relative Oxygen

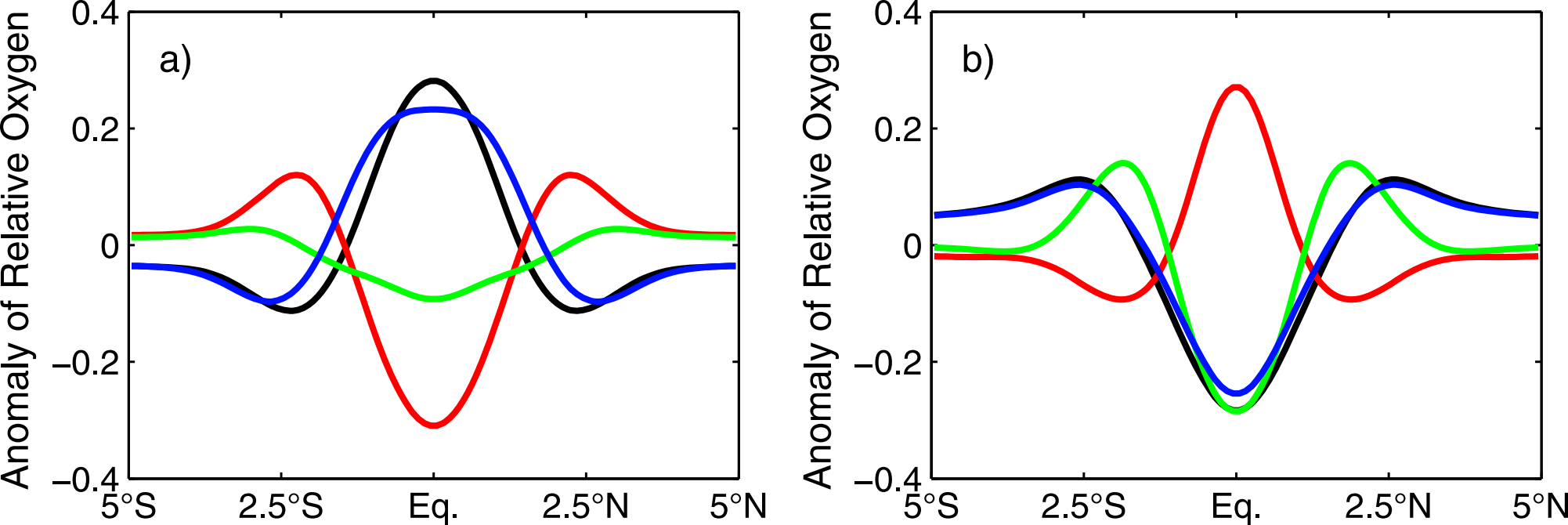
a)
b)
Anomaly of Relative Oxygen
0.4
0.2
0
−0.2
−0.4
5°S
2.5°S
Eq.
2.5°N
5°N

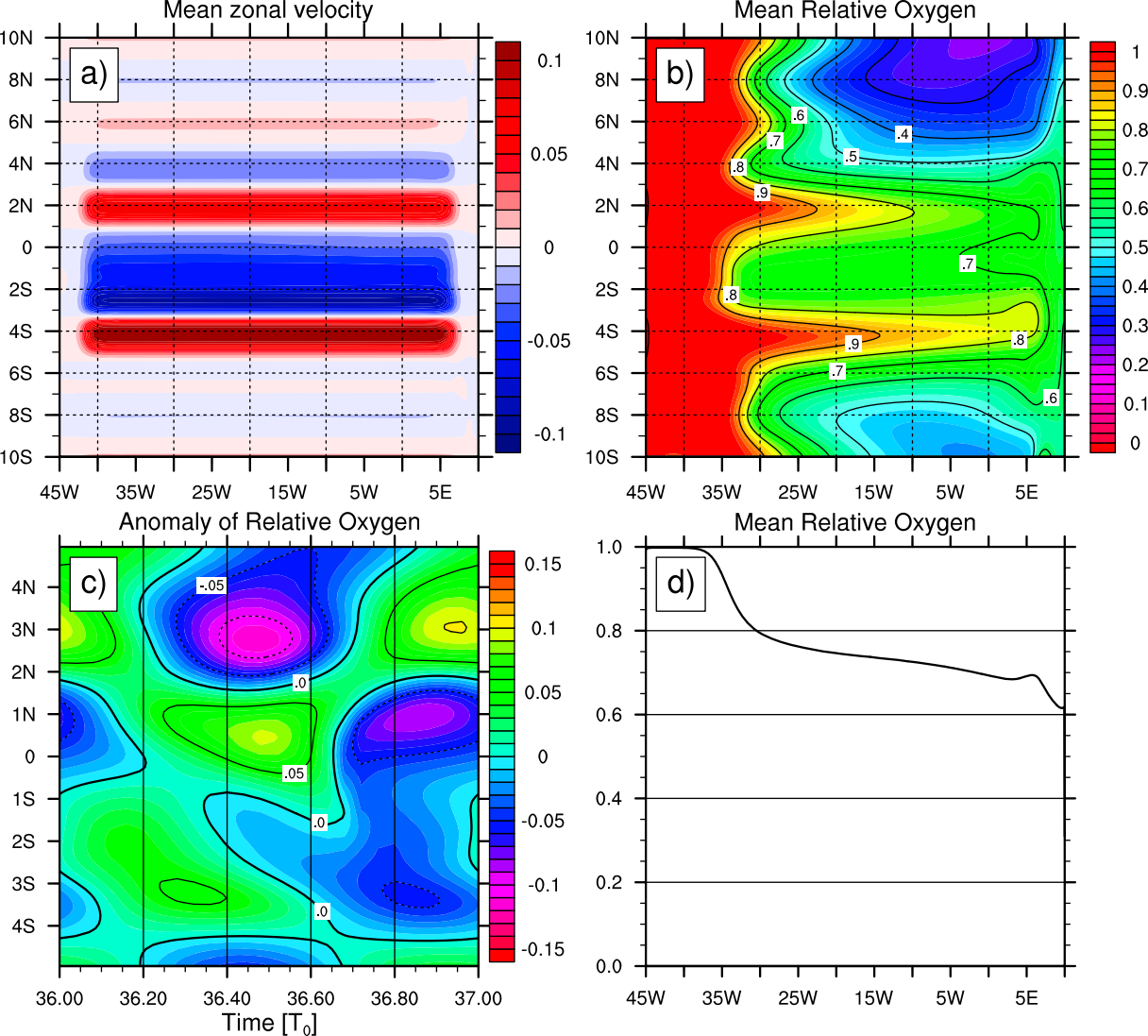
Mean zonal velocity
a)
10N
8N
6N
4N
2N
0
2S
4S
6S
8S
10S
45W
35W
25W
15W
5W
5E
0.1
0.05
0
-0.05
-0.1
Mean Relative Oxygen
b)
.6
.7
.8
.9
.4
.5
.7
.8
.9
.7
.6
1
0.9
0.8
0.7
0.6
0.5
0.4
0.3
0.2
0.1
0
Anomaly of Relative Oxygen
c)
-.05
.0
.05
.0
.0
4N
3N
2N
1N
0
1S
2S
3S
4S
36.00
36.20
36.40
36.60
36.80
37.00
Time [T0]
0.15
0.1
0.05
0
-0.05
-0.1
-0.15
Mean Relative Oxygen
d)
1.0
0.8
0.6
0.4
0.2
0.0
45W
35W
25W
15W
5W
5E

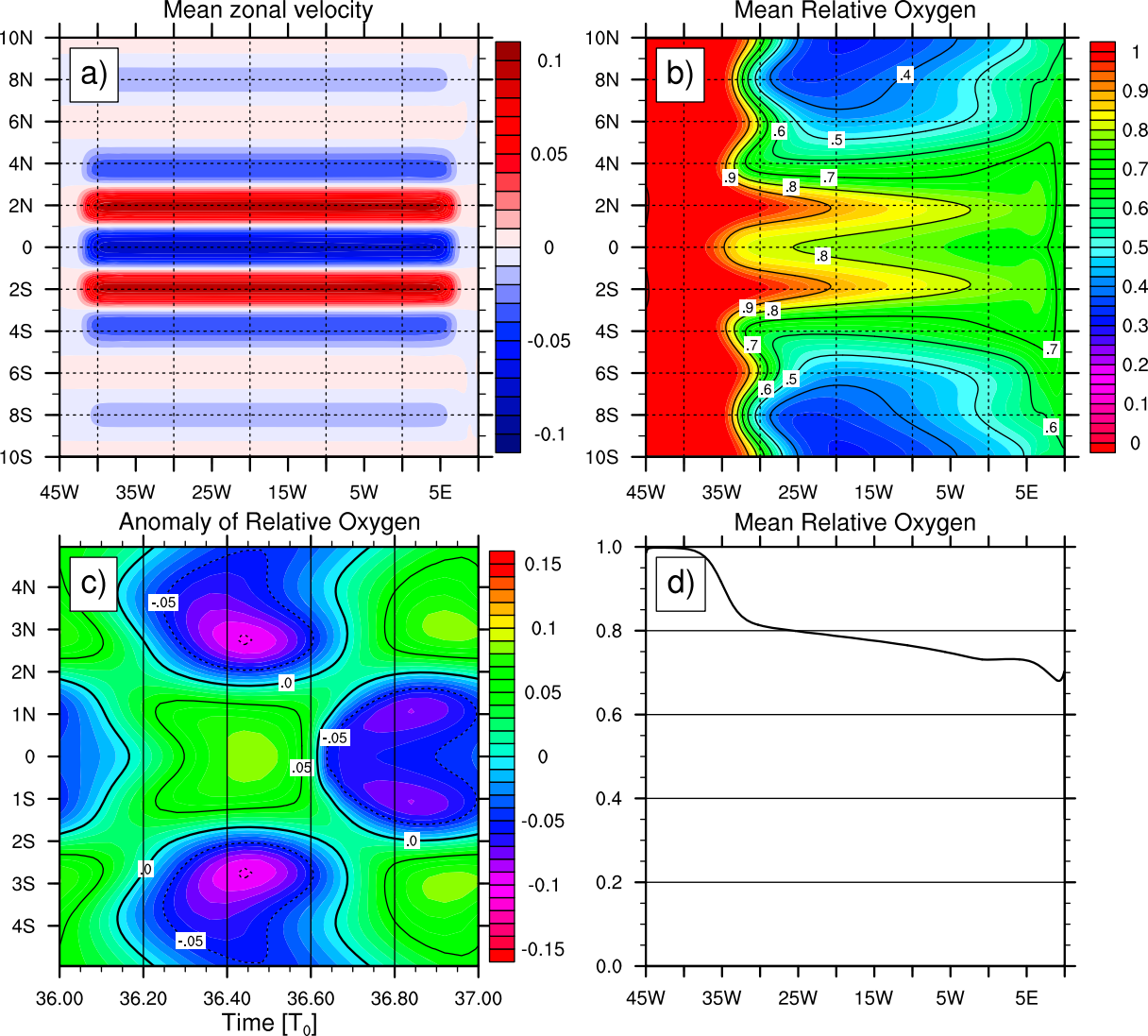
Mean zonal velocity
a)
10N
8N
6N
4N
2N
0
2S
4S
6S
8S
10S
45W
35W
25W
15W
5W
5E
0.1
0.05
0
-0.05
-0.1
Mean Relative Oxygen
b)
.4
.6
.5
.9
.7
.8
.8
.9
.8
.7
.7
.5
.6
.6
1
0.9
0.8
0.7
0.6
0.5
0.4
0.3
0.2
0.1
0
Anomaly of Relative Oxygen
c)
-.05
.0
-.05
.05
.0
.0
-.05
4N
3N
2N
1N
0
1S
2S
3S
4S
36.00
36.20
36.40
36.60
36.80
37.00
Time [T0]
0.15
0.1
0.05
0
-0.05
-0.1
-0.15
Mean Relative Oxygen
d)
1.0
0.8
0.6
0.4
0.2
0.0
45W
35W
25W
15W
5W
5E